A modelling study on tsunami propagation in the Red Sea: Historical events, potential hazards and spectral analysis

J.M. Abril, R. Periáñez*

Dpto. Física Aplicada I, ETSIA, Universidad de Sevilla, Ctra. Utrera km 1, 41013-Sevilla, Spain

ABSTRACT

Keywords:
Red Sea
Tsunami
Numerical simulation
Fluid dynamics
Spectral analysis

This work reports results from numerical simulations of the tsunami triggered by 1995 Nuweiba earthquake, in the Gulf of Aqaba, which are consistent with the available observations. A series of 12 potential tsunamigenic sources are then considered in the Red Sea: related to major submarine earthquakes; volcanism (entry of pyroclastic flows and caldera collapse) and submarine landslides. Numerical simulations have been carried out to solve the spatial distribution of maximum amplitudes of water elevations and currents, and the flooded coastal areas. The peak energy in the simulated events range from 1 kt (1 kt=4.18×10^{12} J) up to 1.5 Mt, and global flood volumes range from 0.005 km3 up to 4.4 km3. A linear correlation can be established between both magnitudes for the set of tsunamis triggered by earthquakes up to 300 kt. Tsunamis triggered by submarine landslides show high directionality, but they occur in deep waters and showed lower impacts on the shoreline, as those triggered by volcanism. A FFT analysis shows that in this basin, tsunamis excite low frequency constituents which can be interpreted as eigenmodes. High frequencies are excited only in the proximity of the source, and the Gulf of Suez excites only those eigenmodes close to the ones of the main basin.

1. Introduction

The geodynamics of the Red Sea area is governed by the interactions between the African, Arabian and Levantine-Sinai plates, being the most relevant geophysical features the Rift of Suez, the Dead Sea shear zone, the Red Sea Rift and the Afar triple junction (Mascle et al., 2000; Bosworth et al., 2005; d'Almeida, 2010). This complex tectonic is responsible for intense earthquake and volcanism activity. Seismicity in the area has been studied, among others, by Foster and Jackson (1998), Bosworth et al. (2005) and Mohamed et al. (2012). Large earthquakes are possible particularly along the Gulf of Aqaba-Dead Sea transform and the Northern Red Sea triple junction point (Mohamed et al., 2012). The major recent events were the 1995 Nuweiba earthquake in the Gulf of Aqaba, with magnitude M_w=7.3 (on June 2015 another event in the same area reached magnitude 5.5); and the 1977 Massawa earthquake in southern Red Sea, with M_w=6.6. The Abu Dabbab seismogenic zone extends offshore in the Red Sea and it is characterized by "cannon" earthquakes, long continued seismic activity, and frequent earthquake swarms. An unique property is that earthquake signals can be heard by humans due to the location of an active fault below a large, rigid, non-deformed block of Precambrian igneous rock, which reaches a depth of ~10 km (El Khrepy et al., 2015).

The Zubair archipelago, along with the Jebel at Tair and the Hanish-Zukur islands are the main exponents of volcanism in the southern Red Sea. From September 2007 to January 2008 the Jebel at Tair eruption event took place, which expelled a bulk volume of 2.2×10^7 m^3 of lava (Xu and Jónsson, 2014). In 2011–2013 submarine eruptions lead to the formation of two new volcanic islands in the Zubair archipelago (Xu et al., 2014).

At the central Red Sea, Miocene evaporites, kilometers in thickness, were deposited during its continental rifting phase, later being covered with hemipelagic sediments of up to some hundred meters thick. Mitchell et al. (2010) identified a remarkable series of structures resembling viscous gravity flows around Thetis Deep, and interpreted as flowage of the evaporites. They found flow-parallel lineaments and extensional faults lying, respectively, parallel and orthogonal to the direction of maximum seabed gradient. Feldens and Mitchell (2015) have identified six salt flows with heights of several hundred meters and widths between 3 and 10 km around Thetis Deep and Atlantis II Deep, and between Atlantis II Deep and Port Sudan Deep. They found flow speeds of several mm/year for the offshore salt flows in certain locations. Mass wasting events have not been identified, although in other scenarios salt tectonics have triggered some giant gravity-driven landslides (Loncke et al., 2009).

The intense earthquake and volcanism activity may have triggered large tsunamis in the past. Thus, Shaked et al. (2004) provided

evidence of a catastrophic sedimentary event at the north-west margins of the Gulf of Aqaba, dated at 2.3 ka BP, that killed the Elat fringing coral reef. The event would have been likely triggered by a tsunami. Salem (2009) reported evidences of paleo-tsunami deposits on a coastal area of the Red Sea north of Marsa Alam city, Egypt.

The Red Sea coastline is mostly a desert and, historically, only very few permanent human settlements have been located there. For such desert regions it is difficult to establish an accurate catalogue of historical tsunamis. The NGDC/WDS Global Historical Tsunami Database (NGD, 2016) records 5 tsunamis in the last millennium. In 1068 a tsunami originated in the Gulf of Aqaba at 34.950°E, 29.500°N, with intensity 4.0 in the NEAMTIC scale. In 1879 a tsunami was triggered by a earthquake with epicenter in the Gulf of Suez (33.000°E, 29.000°N). At Tor, in Sinai, a sea-wave flooded the village. A landslide is a possible source for this tsunami, but there is not any documentation in the historical records (Jordan, 2008). A damaging earthquake occurred in Eritrea in July 1884, with epicenter offshore Massawa (39.600°E, 15.700°N). High sea waves built up in the harbor of this city and the sea flooded the land several times. On March 1969 an earthquake with epicenter in the Gulf of Suez (34.000°E, 27.700°N) affected the islands of Shadwan, Tawila and Gubal. Dead fish and some agitation of the sea were noticed after the main shock.

A strong earthquake, M_w=7.3, occurred in the Gulf of Aqaba on 22 November 1995, with epicenter at 34.75°E, 28.97°N (Baer et al., 2008). In the cities of Aqaba (Jordan) and Eilat (Israel), at the northern reaches of the gulf, a small wave swept the beach according to witnesses (Klinger et al., 1999). Major damage occurred at the city of Nuweiba, where five people died and 11 were injured. Many buildings and the harbor area suffered structural damage, and liquefaction phenomena were also reported (Al-Tarazi, 2000; Klinger et al., 1999). Basta et al. (1996) mentioned that a tsunami 3–4 m high hit Nuweiba harbor. The source parameters of the Nuweiba earthquake have been determined by several independent studies (Klinger et al., 1999; Baer et al., 2008 and references within), which allows numerical simulations of the tsunami propagation.

The numerical modelling of tsunami propagation is a relatively well established methodology which has been validated against recorded data from historical events over the world (Choi et al., 2008; Alasset et al., 2006; Ioualalen et al., 2010; Periáñez and Abril, 2013, 2014a). The main agents triggering tsunamis are earthquakes by geological faults, submarine and sub-aerial landslides, entry of pyroclastic flows and caldera collapse in volcanoes. Reliable modelling strategies have been developed for all of them (Iglesias et al., 2011; Novikova et al., 2011; Okal et al., 2011; Periáñez and Abril, 2014a).

As far as we know, tsunami modelling works have not been previously conducted in the Red Sea area. This paper is aimed at studying the tsunami propagation in these waters by adapting previously tested numerical tools. The characterization of the source parameters for the 1995 Nuweiba earthquake, along with the scarce description of the tsunami effects (as above commented) provide a minimum basis for supporting a modelling exercise. From the available studies on the seismicity in this area, it is possible to construct hypothetical tsunamigenic sources by handling the known focal parameters, namely the epicenter and fault angles. Similarly, from the known main features of the volcanism and salt flows, it is possible to built hypothetical scenarios for the entry of pyroclastic flows, for caldera collapse and submarine landslides. These numerical exercises are expected to provide some insight on the main features of the tsunami propagation in this marine system, which exhibits a quite singular geometry. Results can allow the assessment of regional exposure. Thus, the Red Sea and the gulfs of Aqada and Suez conform long and narrow open basins for which fundamental periods of several hours (within the range of those of the main tidal constituents) are expected (Rabinovich, 2009). Studying eventual wave amplification and resonance effects may be of particular interest for the main cities in the coastal area, and for assessing the potential risks for the Suez

Canal, of great commercial and strategic value (Finkl et al., 2012).

The model is briefly described in Section 2.1 and the different tsunami sources are presented in Section 2.2. Results are described in Section 3. Initially, the simulation carried out for the 1995 Nuweiba Earthquake, for which some observational data exist, is presented (Section 3.1). Then, results on the potential tsunamis triggered by other earthquakes, landslides and volcanic activity are described (Section 3.2). The spectral analysis which has been carried out is described in Section 3.3. Some general discussion on tsunami hazard in the Red Sea closes the paper (Section 3.4).

2. Methods

2.1. Model description

The tsunami propagation model is based on the 2D depth-averaged barotropic shallow water equations, which describe the propagation of surface shallow water gravity waves. The numerical tool has been adapted from previous works, and it has proved to be a very robust computational tool (Periáñez and Abril, 2013, 2014a, 2014b).

The two components of the depth-averaged water current(u, v, in the east-west and south-north directions, respectively), along with the water surface elevation above the reference level, ζ, are given by the equations for conservation of mass and momentum:

$$\frac{\partial \zeta}{\partial t} + \frac{\partial}{\partial x}(Du) + \frac{\partial}{\partial y}(Dv) = 0 \tag{1}$$

$$\frac{\partial u}{\partial t} + u\frac{\partial u}{\partial x} + v\frac{\partial u}{\partial y} + g\frac{\partial \zeta}{\partial x} - \Omega v + \frac{\tau_u}{\rho D} = A\left(\frac{\partial^2 u}{\partial x^2} + \frac{\partial^2 u}{\partial y^2}\right) \tag{2}$$

$$\frac{\partial v}{\partial t} + u\frac{\partial v}{\partial x} + v\frac{\partial v}{\partial y} + g\frac{\partial \zeta}{\partial y} + \Omega u + \frac{\tau_v}{\rho D} = A\left(\frac{\partial^2 v}{\partial x^2} + \frac{\partial^2 v}{\partial y^2}\right), \tag{3}$$

where h is the undisturbed water depth, ζ is the displacement of the water surface above the undisturbed sea level measured upwards, $D = h + \zeta$ is the total water depth, Ω is the Coriolis parameter ($\Omega = 2w\sin\lambda$, where w is the Earth rotational angular velocity and λ is latitude) and A is the horizontal eddy viscosity. τ_u and τ_v are friction stresses which have been written in terms of a quadratic law:

$$\tau_u = k_f \rho u \sqrt{u^2 + v^2} \quad \tau_v = k_f \rho v \sqrt{u^2 + v^2} \tag{4}$$

where k_f is the bed friction coefficient. All the equations are numerically solved using explicit finite difference schemes (Kowalik and Murty, 1993) with second order accuracy. In particular, the MSOU (Monotonic Second Order Upstream) is used for the advective nonlinear terms in the momentum equations.

Values of k_f=0.0025 and A=10 m^2/s have widely proved their use in models for tide and tsunami propagation (e.g., Periáñez and Abril, 2013, 2014a, 2014b).

The model domain (Fig. 1) extends from 32.0°E to 45.0°E, and from 10.0°N to 30.5°N, with a spatial resolution of 60 s of arc. A higher resolution sub-domain has been used for the northern Red Sea, which is 30 s of arc resolution, and extends from 32.0°E to 39.0°E and from 24.0°N to 30.0°N. The bathymetries have been obtained from the GEODAS and GEBCO08 (60 and 30 s of arc respectively) databases, available on-line. Due to the wide range in latitude, the Coriolis parameter and the spatial resolution in longitude are allowed to vary with λ. The continuity equation was appropriately written to account for such variation in Δx. Time steps of 1 s and 2 s were fixed for the 30″ and 60″ mesh resolutions, respectively.

A gravity wave radiation condition is used for sea surface elevation (Periáñez and Abril, 2014a) along the open boundary in the southeastern side of the domain. A wetting/drying algorithm is implemented following the numerical scheme described in Kampf (2009). It allows the calculation of runup over land. Still waters (zero water elevations and velocities over all the domain) are used as initial conditions in all
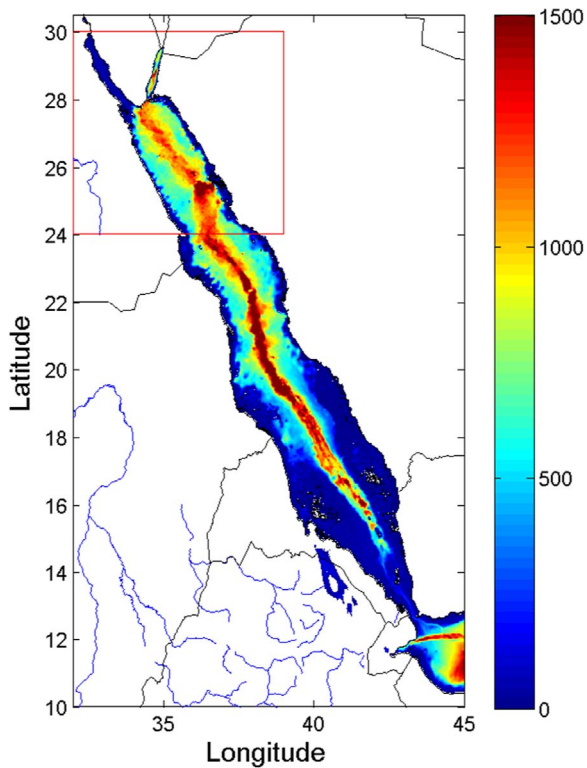
Fig. 1. Computational domain for the 2D simulations with a spatial resolution of 60 s of arc. The square delimits a higher resolution domain which uses 30 s of arc. Depths are taken from GEGCO08 and GEODAS databases. Scale color-bar in m, measured positive below the present sea level.

the domain except for those areas affected by the deformation in the free surface induced by volcano caldera collapse, or by submarine earthquakes triggered by geological faults.

For tsunamis produced by earthquakes in geological faults, the sea-floor deformation produced by the earthquake is computed using the classical Okada formulae (Okada, 1985). Inputs for this equation are fault plane strike, rake, dip, slip, location, length and width, as well as seismic moment and rigidity. The standard procedure assumes that such deformation is instantaneously transferred to the free water surface, and it is imposed as the initial conditions for the numerical simulation (see, for instance, Ioualalen et al., 2010; Abril et al., 2013).

Due to the exploratory character of this study, the simplest approach by Harbitz (1992) and Cecioni and Bellotti (2010) has been adopted to simulate tsunamis triggered by submarine landslides. The slide can be described as a solid body whose downslope movement locally modifies the bathymetry and induces changes in the level of the overlapping waters, which propagate as gravity waves. The adopted geometry is a box of length L, width B and maximum thickness Δh, and

with an exponential smoothing over a distance S in the front and rear and $B/2$ on the flanks. The resulting volume is $V = 0.90B\Delta h(L + 0.90S)$ (Harbitz, 1992). The maximum velocities and duration of the displacement can be estimated from the slope, maximum height and friction and drag coefficients (Harbitz, 1992). The two-slope kinematic model by Periáñez and Abril (2014a) has been adopted. Applications of this model can be found in such reference and in Abril et al. (2013), Abril and Periáñez (2015).

Tsunamis generated by a pyroclastic flow into the sea can be modelled as a particular case of a submarine landslide in which the initial length of the slide is zero and it increases in time as the pyroclastic flow is entering the sea. The high initial velocity, U_O, decreases to zero as the flow completes a displacement R_2. These parameter values can be estimated following the methodology by Novikova et al. (2011). Applications of this model can be found in this reference and in Periáñez and Abril (2014a).

For modelling a volcano caldera collapse, the methodology by Novikova et al. (2011) has been adopted. The initial water level corresponds to the depth of the caldera formed. Thus, the initial water displacement is negative (i.e., downwards). Alternatively, the formula described by Torsvik et al. (2010) for under-water explosions could be used.

2.2. Tsunamingenic sources in the Red Sea

2.2.1. The 1995 Nuweiba Earthquake ($M_w = 7.3$)

The Gulf of Aqaba lies at the southern segment of the Dead Sea Fault (DSF) system. It is 180 km long and 10–25 km wide, resulting from the succession of three pull-apart basins: the Dakar Deep, the Aragonese Deep and the Elat Deep. Depths within the gulf reach 1800 m deep in places, and it is surrounded by the high mountain ranges of Sinai and Hedjaz. The M_w 7.3 1995 Aqaba earthquake is the largest instrumentally recorded earthquake along the DSF (Klinger et al., 1999). A description of its effects on the coastal areas of the Gulf of Aqaba and the cities of Aqaba, Eilat and Nuweiba can be found, among others, in the work by Klinger et al. (1999), and they have been summarized in the Introduction section. These authors reported small tsunami waves at Aqaba and Eilat. Mention to high tsunami waves, up to 3–4 m in the Nuweiba harbor is found in the work by Basta et al. (1996), as reported by Salem (2009).

The epicenter of the earthquake was offshore. The source parameters have been studied by different authors based on seismology and InSAR methods, as summarized by Baer et al. (2008). These authors provided the more updated estimation involving a single event with a variable slip of 0–3 m. Their results, with the maximum slip value of 3 m have been used to define the source F1 in this study (Table 1). Klinger et al. (1999) suggested a sequence of three events, with 2.5 m slip for the largest one, but without quantifying the fault width. Source F1b in Table 1 is a version of F1 with this lower slip value. The surface deformations, estimated from the formula of Okada (1985) lead to a

Table 1
Fault parameters used in simulations. Geographical coordinates correspond to the fault center. References: [1] Baer et al. (2008) [2] Klinger et al. (1999), Baer et al. (2008). Hypothetical faults based on focal mechanisms of recorded earthquakes and imposed values for length, wide and slip: [3] Mohamed et al., 2015; events 1–2004 (their Table 2) and 3–2006 (their Table 3); [4] Foster and Jackson (1998) events 670313, 771228 and 930313 and 800114, with tuned parameters; [5] This is a pure synthetic source. For the hypothetical faults the rake angle has been tuned to zero in the application of the Okada formula to enhance the vertical displacement.

Tsunami	ϕ_E°	λ_N	Length (km)	Wide (km)	Slip (m)	Strike (°)	Dip (°)	Rake (°)	Reference
F1 (Nuweiba 1995)	34.75	28.97	58.5	30.0	3.0	197.5	67.0	−4.0	[1]
F1b (Nuweiba 1995)	34.75	28.97	58.5	30.0	2.5	197.5	67.0	−4.0	[2]
F2 (Gulf of Suez)	33.10	28.47	50.0	20.0	8.0	308.0	53.0	−63.0	[3]
F3 (South Sinai)	34.62	27.39	80.0	30.0	8.0	125.0	52.0	−69.0	[3]
F-RS1 (670313)	38.75	19.68	160.0	60.0	10.0	309.0	45.0	−100.0	[4]
F-RS2 (771228)	40.28	16.66	120.0	40.0	10.0	106.0	66.0	−171.0	[4]
F-RS3 (930313)	38.85	19.67	180.0	80.0	12.0	144.0	40.0	−84.0	[4]
F-RS4 (800114)	40.34	16.52	200.0	90.0	14.0	24.0	30.0	−9.0	[4]
F-RS5	34.62	27.35	150.0	60.0	14.0	125.0	52.0	0.0	[5]

maximum (gravitational potential) energy for the triggered tsunamis of 1.24 and 0.86 kt (1 kt=4.18×10^{12} J) for F1 and F1b, respectively.

2.2.2. Source parameters for hypothetical tsunamis triggered by submarine earthquakes

Table 1 reports fault parameters for a set of seven tsunamigenic sources used in simulations. Epicenter and fault angles are based on the seismicity studies reported by Mohamed et al. (2015) -events 1–2004 and 3–2006, and Foster and Jackson (1998) - events 670313, 771228, 930313 and 800114. This selection of sources is linked to the major earthquakes events and it covers the main seismic zones within the studied domain. The values for length, width and slip have been imposed with the criteria of generating energetic events able to propagate over large areas within the Red Sea. In order to enhance the vertical displacement, the rake angle has been tuned to zero degrees in the application of the Okada formula. Sources F2 and F3 have been simulated with the 30-seconds resolution mesh, and sources F-RS1 to F-RS5 with the 1-min resolution mesh.

2.2.3. Tsunamis triggered by pyroclastic flows and caldera collapse

The Jebel at Tair volcano has been selected as the scenario for these tsunamigenic sources. The volcanic island has an ellipsoidal shape with a major diameter of 4.4 km. The eruption event of September 2007 has been well described by Xu and Jónsson (2014). It expelled 2.2×10^7 m^3 of lava with two main flows in the E-NE and W-SW directions. Here we explore the effects of a more severe eruption, producing a pyroclastic flow with a total volume of 5.4 km^3, entering into the sea at the northern area of the Jebel at Tair volcano. The flow is 3.6 km wide (~$2\Delta x$), a thickness of 60 m, and it is directed to 323° (measured clockwise from the North). Following the modelling approach by Novikova et al. (2011), the initial velocity of the flow was estimated as 68 m/s, and its duration was 0.32 h. The Jebel at Tair rises on a topographic low in the Red Sea Rift. The front of the flow would be captured within this geological bowl, completing a maximum run-out distance of 25 km. A sinus function has been adopted for the attenuation of the flow speed. This scenario can be compared with those reported by Novikova et al. (2011). Thus, the total volume of pyroclastic flow in the 1883 Krakatau eruption was 20 km^3 with a maximum velocity of 150 m/s and a thickness of 20 m. These magnitudes took values of 20 km^3, 200 m/s and 80 m for the 1815 Tambora eruption.

The caldera collapse is assumed to be produced in the northern area of the volcanic island, with a total volume of 5.0 km^3 and a mean depletion depth of 250 m. This figure can be compared with the 19–34 km^3 collapse modelled by Novikova et al. (2011) for the Late Bronze Age eruption of Thera.

2.2.4. Tsunamis triggered by submarine landslides

Two hypothetical mass wasting events have been considered, located at the front of two salt flow lobes identified by Feldens and Mitchell (2015) in the Thetis Deep and the Atlantis II Deep (their regions C and D, respectively). From the detailed relief image of multibean data it is possible to extract realistic values for the front position, topographic slopes, slide width, runout distance and direction of displacement, which are completed with estimates of length, smoothing distance, and maximum thickness to generate tsunamigenic events involving 21.0 and 26.5 km^3, respectively. Table 2 summaries the geometric and kinematic parameters for this two submarine landslides. The slide SL2 is a version of SL1 with a larger runout distance.

3. Results and discussion

3.1. The 1995 Nuweiba earthquake

Fig. 2 shows two snapshots with the computed instantaneous water surface elevations 15 and 60 min after the 1995 Nuweiba earthquake using the source parameters F1 (Table 1). Along the deepest central axis of the Gulf, the speed of gravity waves can surpass 450 km/h. Although it is lower in the shallower coastal areas, in this narrow water body the tsunami signal reaches Nuweiba and Haql in less than three minutes (Fig. 3), and after seven minutes it is perceived at Aqaba. The reflected waves then produce multiple interferences within the gulf, and the sea becomes stormy.

Fig. 3 shows the computed time series of water elevations for five selected locations along the gulf shoreline (they are labelled in Fig. 2). The first wave at Aqaba, at the northern reaches of the gulf, has an amplitude of 0.8 m (0.7 when using the alternative source F1b from Table 1). Then, waters recede and a new series of waves hit the shoreline at intervals of roughly 30 min. At Nuweiba, the first wave is 1.5 m height (1.3 with source F1b). At this location the maximum range between high and low water levels reaches 2.9 m. The tsunami signal is noisier, with high frequency constituents, but as time goes on, the ~30 min period becomes dominant. A similar trend is observed in Haql, in the eastern shore of the Gulf of Aqaba, but with a maximum amplitude of 0.6 m, and with a higher contribution of high frequency constituents. The tsunami signal in Nabq, close to the gulf mouth, is smoother, similar in amplitude to that of Haql, and both tend to run in phase. The signal at Sherm, at southern Sinai and out of the Gulf of Aqaba, has a maximum amplitude of only 7 cm.

Fig. 4 shows the computed maximum amplitude for water elevations and water currents 6 h after the 1995 Nuweiba earthquake. Amplitudes of 1 m can be encountered in the western shore of the Gulf, around the area of Nuweiba, and in the opposite eastern coasts, being the last directly affected by the initial seafloor deformation. Moderately high amplitudes (over 0.8 m) are found in the northern area of the Gulf and in some scattered embayments. Out of the Gulf of Aqaba the impact of the tsunami is very week. As seen in the same figure, water currents over 0.4 m/s are found only along few coastal areas and in the southern gulf. Those land grid-cells that at any time become flooded by the tsunami appear as open red circles in Fig. 4 (the size has been exaggerated). There are only 10 places, which correspond to coastal areas with mean land elevation around 1 m above sea level. They are flooded by water laminae with thickness ranging from 0.1 up to 1.1 m. It is worth noting that tides in the Gulf of Aqaba have an amplitude of the order of 0.6 m, with surface water currents that rarely surpass 20 cm/s (Monismith, 2004; Ahmed et al., 2012),

Although with a stormy sea, the characteristic pattern of standing waves emerged along the gulf axis. Nodal lines which separate areas with high and low water levels (Fig. 2) appear with a configuration close to node n=2 for an open-mouth rectangular basin ($L = \frac{5}{4}\lambda_T$, where λ_T is the wavelength of the tsunami; see Rabinovich, 2009). Thus, with the known values for the length of the Gulf of Aqada (L=180 km) and its axial depth (H~1800 m), it is possible to estimate a period $T_2 \sim 0.5$ h ($T_n = 4L/[(2n + 1)\sqrt{gH}]$; Rabinovich, 2009). The time series in Fig. 3 were used to evaluate the power spectral density (proportional to the energy spectral density) from FFT analysis (Sahal et al., 2009; Periáñez and Abril, 2014b). Results are shown in Fig. 5 for four of the selected locations. A major peak appears in all cases for a period of 0.55 ± 0.05 h (the range corresponds to half the time window resolved by the applied Matlab FFT algorithm, as in Periáñez and Abril, 2014b), which compares well with the previous estimate. A period of 1.0 ± 0.2 h is well resolved in Aqaba and Naql sites, which fits to the theoretically estimated value of $T_1 \sim 0.9$ h. A period of 0.38 ± 0.02 h is observed at three of the sites, which corresponds to $T_3 \sim 0.4$ h. At Nuweiba the tsunami signal has a high intensity, and it is possible to solve the period 0.30 ± 0.2 h (T_4). The fundamental period $T_0 \sim 2.7$ h is observed in all the cases, although with a poorer resolution.

Table 2

Source parameters for hypothetical tsunamis triggered by submarine landslides in central Red Sea. They are defined as in Harbitz (1992) with kinematics after Periáñez and Abril (2014a). The slide volume is $V = 0.9B\Delta h(L + 0.9S)$; B, width; L, length; S, smoothing distance; Δh, maximum thickness. Slide direction is measured clockwise from the north. The position refers to the initial front location.

Landslide	Geometrical parameters					Position		Dir	Kinematics					
	L (km)	S (km)	B (km)	Δh (m)	V (km³)	ϕ_E°	λ_N°	θ°	R_1 (km)	α_1 (°)	$U_{max,1}$ (m/s)	R_2 (km)	α_2 (°)	$U_{max,2}$ (m/s)
SL1	9.0	3.0	10.0	200	21.0	37.819	22.444	245	4.5	6.0	50.0	4.5	1.8	37.8
SL2	9.0	3.0	10.0	200	21.0	37.819	22.444	245	6.0	5.0	50.0	10.0	1.8	37.8
SL3	12.0	3.0	10.0	200	26.5	38.280	20.572	190	7.5	4.5	50.0	7.5	4.5	50.0

3.2. Hypothetical scenarios for tsunamis in the Red Sea

3.2.1. Tsunamis triggered by submarine earthquakes in geological faults

The tsunami F2 (Table 1) occurs in the central Gulf of Suez, where the seafloor deformation injects 7.7 kt into the water column as initial potential gravitational energy. Fig. 6 shows the computed maximum amplitudes for water elevations and water currents after a simulation time of 6 h. Water elevations surpass 3 m in the area over the geological fault and they produce noticeable flooding in the adjacent shoreline, with runups over 3 m (yellow circles in this figure) and water currents over 1 m/s. The impact of the tsunami decreases northwards, but an amplification phenomena is observed around the Port of Suez where the coastal zones are flooded with a water laminae of some 0.5 m. South of the source area the amplitudes and velocities are also high, particularly along the eastern shoreline. The tsunami impacts are negligible out of the Gulf of Suez.

Fault F3 (Table 1) is located southeast of the Sinai Peninsula, and the associated tsunami has an initial energy of 18.8 kt. It shows a high directionality normal to the fault strike. In the directly impacted coasts, this tsunami produces runups over 3 m (Fig. 7). High waves propagate along the shorelines, producing floods over 1.0 m at many places. Computed time series of water elevations at some selected locations after tsunamis F2 and F3 are shown in Fig. S-1, in Electronic Supplementary Material (ESM).

Figs. 8 and 9 show the computed maximum amplitudes for water elevations and currents for the two most energetic earthquakes, F-RS3 and F-RS4 (Table 1), with initial energies of 300 kt and 550 kt, respectively. Tsunami F-RS3 produces high water amplitudes in a wide band of the Central Read Sea south of the line defined by the cities of Sudan and Yidda, where the coastal areas are flooded with runups over 3 m. Elevations over 1 m propagate along the shorelines flooding areas with low topographic elevation. An amplification phenomena is observed in the northern shoreline of the main basin and in the Gulf of Aqaba, with water elevation amplitudes around 0.8 m. This tsunami induces strong currents in the shallow and relatively distant areas of the Farasan Islands and the Dahlak Archipelago. Tsunami F-RS4, has its epicenter in the Southern Red Sea, at only 20 km from the northern Dahlak Archipelago, and 150 km from the Farasan Islands. Thus, it strongly impacts these archipelagos, where it produces high water currents and noticeable floods. At Massawa, the first wave is 2.4 m high. North of Sudan water elevations are negligible, although an amplification effect appears again in the Gulf of Aqaba, with amplitudes over 0.5 m. Water currents of $0.15-0.20$ m/s run along most of the shoreline of the Red Sea. There is a slight amplification at the entrance of the Gulf of Suez. Tsunami F-RS2 (not shown) has the same epicenter than F-RS4, but different geometrical and focal parameters. Its initial energy is 39.2 kt, which is mostly dissipated around the source area and in the eastern edge of the adjacent rift. Some flooding appears along the northern Dahlak Archipelago and in nearby shore of Eritrea.
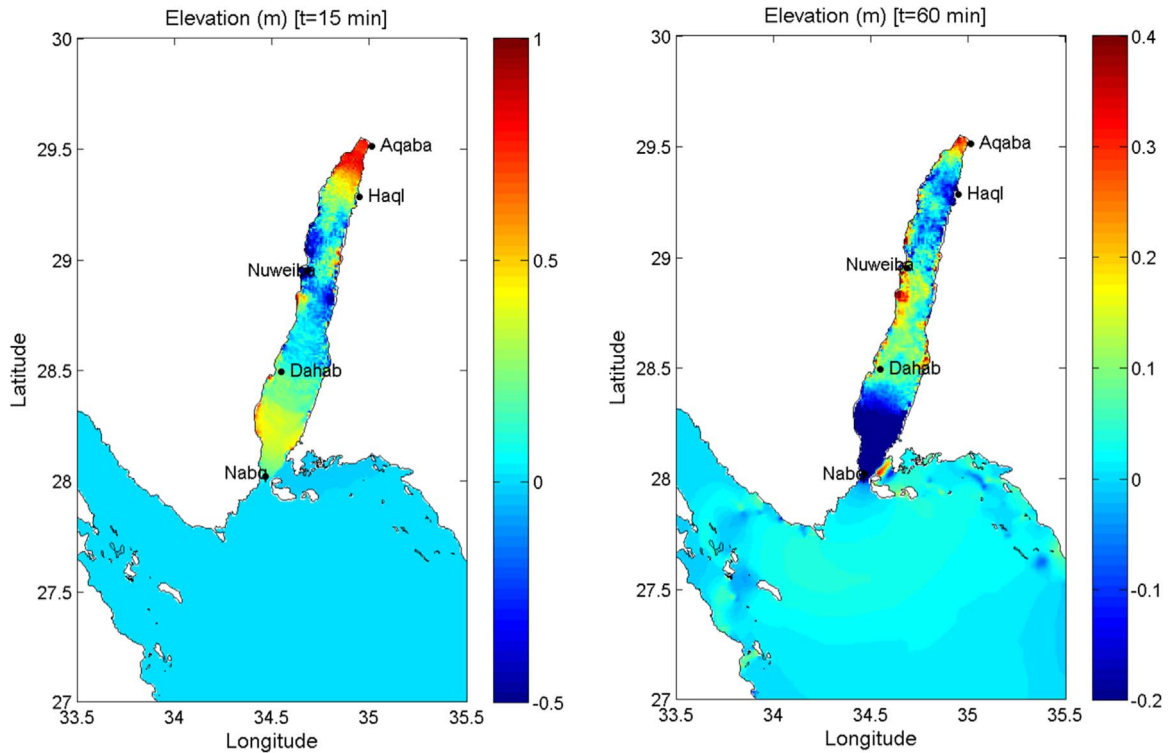

Fig. 2. Computed instantaneous water surface elevations 15 and 60 min after the 1995 Nuweiba earthquake (source parameters F1 in Table 1).
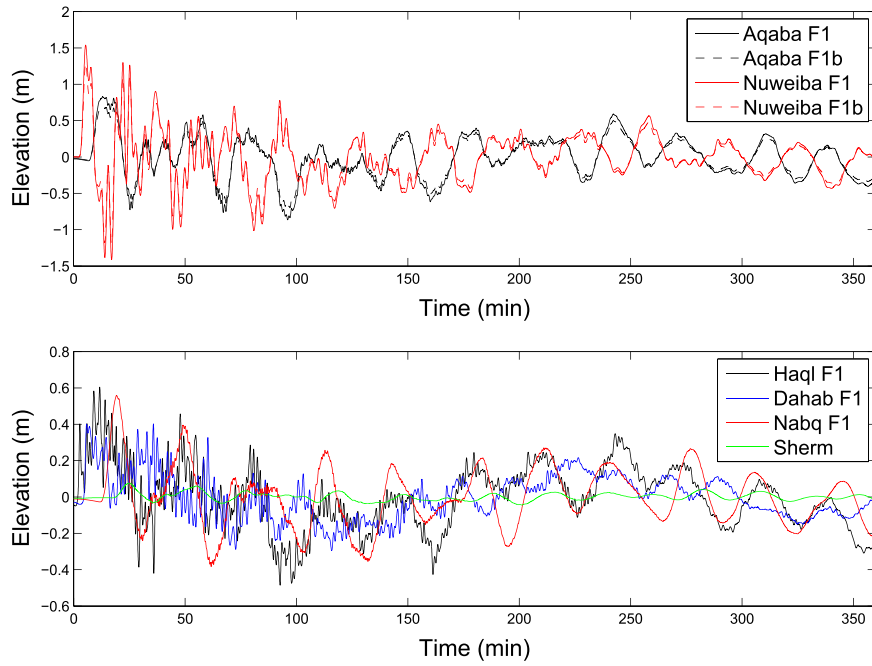
Fig. 3. Computed time series of water elevations at five selected locations (see map in Fig. 2) after the 1995 Nuweiba earthquake.

Figures S-2 and S-3 (in ESM) show the computed maximum amplitude of water elevations and water currents for tsunamis F-RS1 and F-RS5, respectively. Their initial gravitational potential energies were 130 kt and 215 kt, respectively. F-RS1 generates high water elevation amplitudes in the Central Red Sea, and high water currents which run along the shorelines, flooding areas around Yibdda and Port Sudan (Fig. S-2). The tsunami F-RS5 strongly impacts all the regions in Northern Red Sea and produces runups over 1.0 m along the shoreline down to Yibdda and Port Sudan (Fig. S-3).

The total volume of seawater flooding the coastal areas can be estimated by multiplying the maximum water height at each flooded grid-cell by its surface. It was (in km^3) 0.011, 0.005, 0.150, 0.330, 2.215, 0.391, 4.447, 3.449 and 3.691 for tsunamis F1, F1b, F2, F3, and F-RS1 to F-RS5, respectively. A linear correlation can be established at 99% confidence level between flooded volume and energy for this set of tsunamis triggered by submarine earthquakes with energies up to 300 kt (e.g., excluding F-RS4). The fitted parameter value for the slope was of 0.0157 ± 0.0006 km^3/kt. This is an empirical relationship which
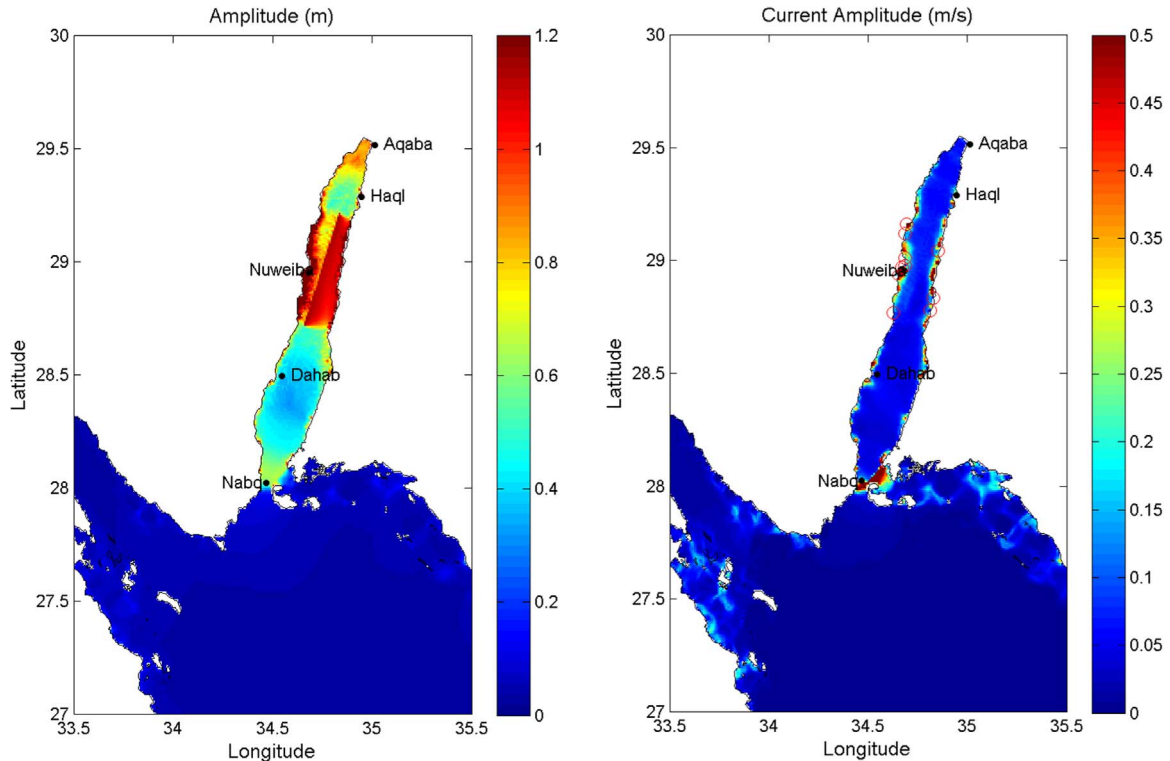

Fig. 4. Computed maximum amplitude for water elevation and water currents due to the 1995 Nuweiba tsunami. Red open circles correspond to those coastal areas being flooded by a water laminae with thickness ranging from 0.1 up to 1.1 m.
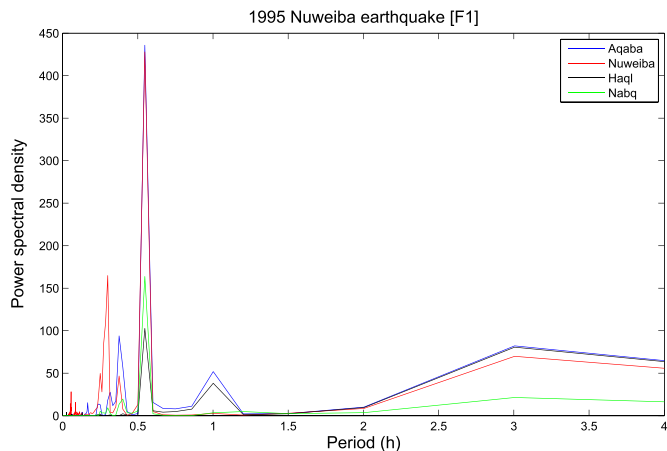
6

Fig. 5. Computed power spectral density (using FFT) from time series of water elevations (Δt = 1.0 s; time-series length 6 h) at a set of selected locations (see Fig. 2).

holds for the studied domain and for this particular set of tsunamis. It can be used with care, along with the tsunami dispersion patterns shown in the previous figures, to get a first proxy to the potential tsunami impacts.

3.2.2. Tsunamis triggered by pyroclastic flows and caldera collapse

As the pyroclastic flow enters into the sea it transfers potential and kinetic energy to the water column. A peak energy of 240 kt is achieved after 7 min. Later energy dissipation becomes dominant. The flow descends towards a topographic low where it is trapped. Thus, the triggered tsunami produces a rather local impact. High values for water currents are found in the shallow areas of the surrounding archipelagos, where some flooded sites also appear (Fig. 10). The total volume of seawater flooding the coastal areas was 0.622 km³, six times lower than the expected from a earthquake-triggered tsunami with equivalent energy.

The caldera collapse triggers a tsunami with an initial energy of 1.5 Mt, but its effects remain constrained to the Southern Red Sea and they are comparable to those produced by the entry of pyroclastic flows

(Fig. 11). Indeed, the total flooded volume was 0.434 km³.

3.2.3. Tsunamis triggered by submarine landslides

Submarine landslides are very energetic events. The tsunamis triggered by SL1 (Table 2) transfers a peak energy of 390 kt to the ocean. It is only slightly higher for SL2 (400 kt), which has a larger runout distance. The tsunami SL3 is even more energetic, with a peak energy of 1.0 Mt. These simulated tsunamis show a strong directionality and rather local impacts (Figs. 12 and S-4 -in ESM). Thus, for SL3 most of the tsunami energy is directed towards the coast around Port Sudan, where a noticeable flooding is produced. At this location the first wave reaches 4.9 m high. Flooding is also produced in the opposite shoreline, around the site of Yidda (see Fig. S-4, ESM). The total flooded volumes were (in km³) 0.260, 0.325 and 1.415 for landslides SL1 to SL3, respectively. They are one order of magnitude lower than those expected from earthquake-triggered tsunamis with equivalent energy.

3.3. Spectral analysis

The energetic events F-RS1, F-RS4 and F-RS5, with epicenters in the Central, Southern and Northern Red Sea, respectively, have been used to generate time series of water elevations for a set of 15 synthetic gauges distributed along the shoreline (given in Table 3 and depicted in Figs. 4 and 9). The time series cover are 24 h long with a time step of 2 s. They served to evaluate the power spectral density from FFT analysis and to identify the periods of the major constituents (Periáñez and Abril, 2014b). Results are shown in Fig. 13 for all locations in Table 3.

The three tsunamis are able to excite a low frequency constituent with period 8 ± 2 h in most of the places. Periods of 4.8 ± 0.4 h and 3.0 ± 0.3 h are also ubiquitous. These figures roughly fit the harmonic sequence with $n = 1,2,3$ from a model of a rectangular open-mouth basin with length ∼2000 km and uniform depth ∼1150 m ($T_n = 4L/[(2n + 1)\sqrt{gH}]$; Rabinovich (2009)). The fundamental period of ∼21 h cannot be resolved with this numerical experiment. For the sake of comparison, Fig. 13 plots the periods predicted by this simple model for $n = 1 - 5$ and $n = 9$. High frequencies (low values for periods)
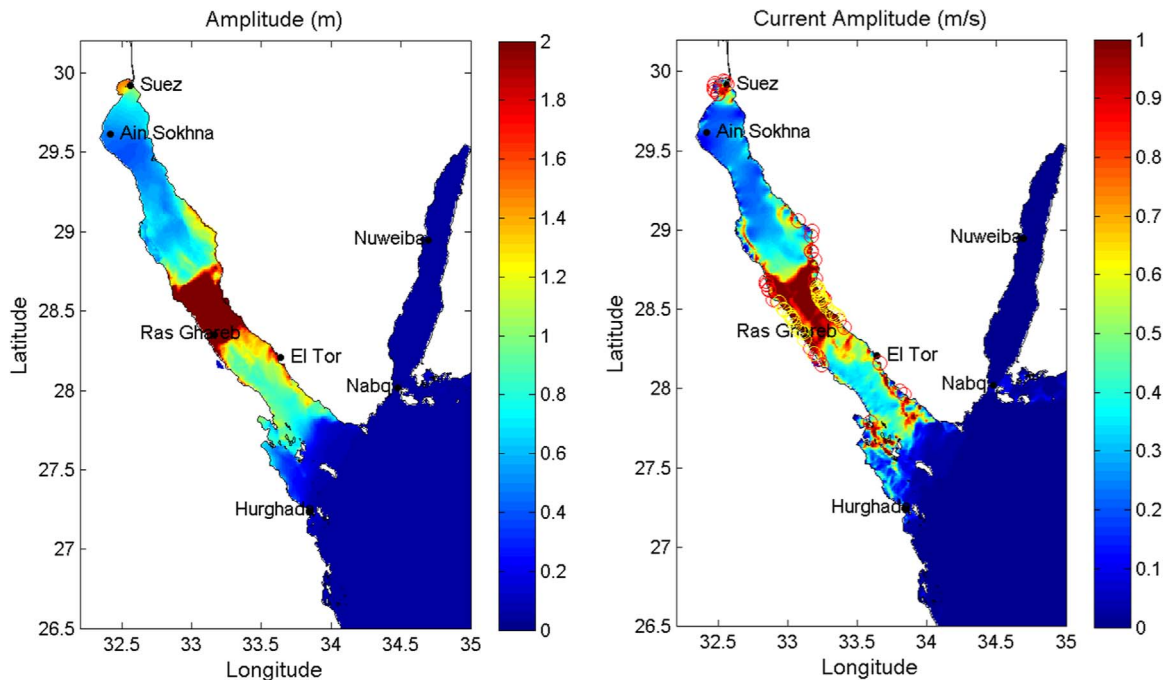

Fig. 6. Computed maximum amplitude for water elevation and water currents due to the F2 tsunami (Table 1). Those land grid-cells flooded with runups in the range of 1–3 m and higher than 3 m are depicted as open red and yellow circles, respectively (the size of the circles has been exaggerated).
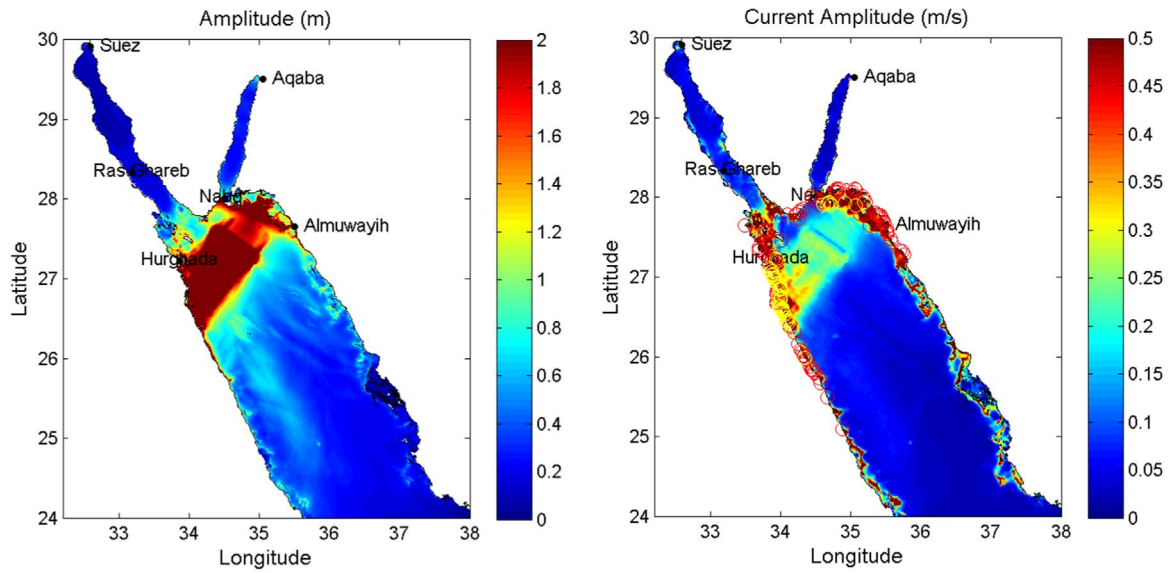
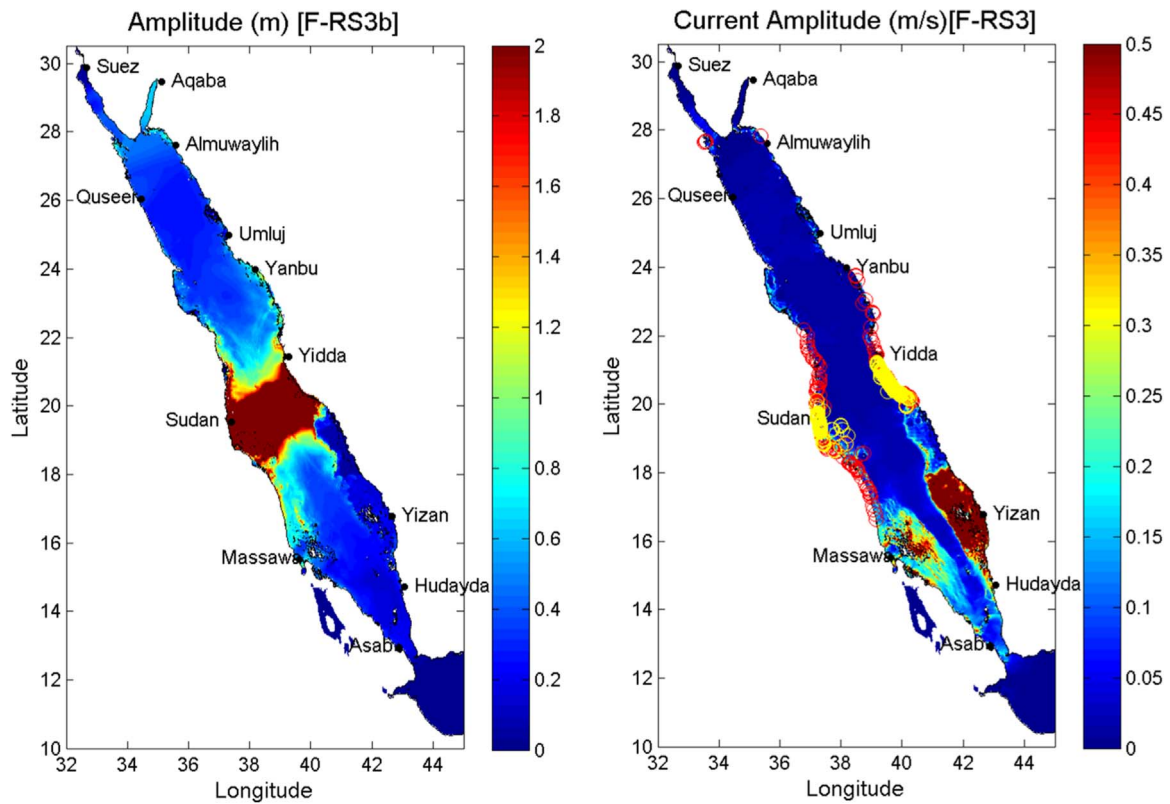**Fig. 7.** As Fig. 6, but for the tsunami F3 (Table 1).

Fig. 8. As Fig. 6, but for tsunami F-RS3 (Table 1).

are excited only in places relatively close to the earthquake epicenter. The deep Gulf of Aqaba (gauges 1–2) follows the trend of the main Red Sea basin, while the shallow Gulf of Suez (gauges 4–5) shows a different behavior. In this case only those eigenmodes which are close to the frequencies of the main basin are excited.

3.4. Discussion on tsunami hazards in the Red Sea

The 1995 Nuweiba earthquake has been the largest instrumentally recorded earthquake along the DSF. Despite the proximity to the epicenter, major damages in Nuweiba were due to the direct effects of the earthquake, with little or null reference to tsunami waves.

The Aqaba and Suez gulfs are long and narrow water-bodies. Tsunami waves reach the shoreline quickly, where they dissipate most of the energy. This limits any potential long distance effects. The same is applicable to the main Red Sea basin.

The few historical tsunami events recorded in the last millennium refer to some rather local impacts. The 12 potential tsunamigenic sources considered in this study include events with different peak energies, but all of them are one of two orders of magnitude more energetic than the 1995 Nuweiba tsunami. Although linked to potential tsunamigenic sources (submarine earthquakes, landslides and volcanos) their probability of occurrence cannot be assessed from historical records, although it can be guessed as very low.
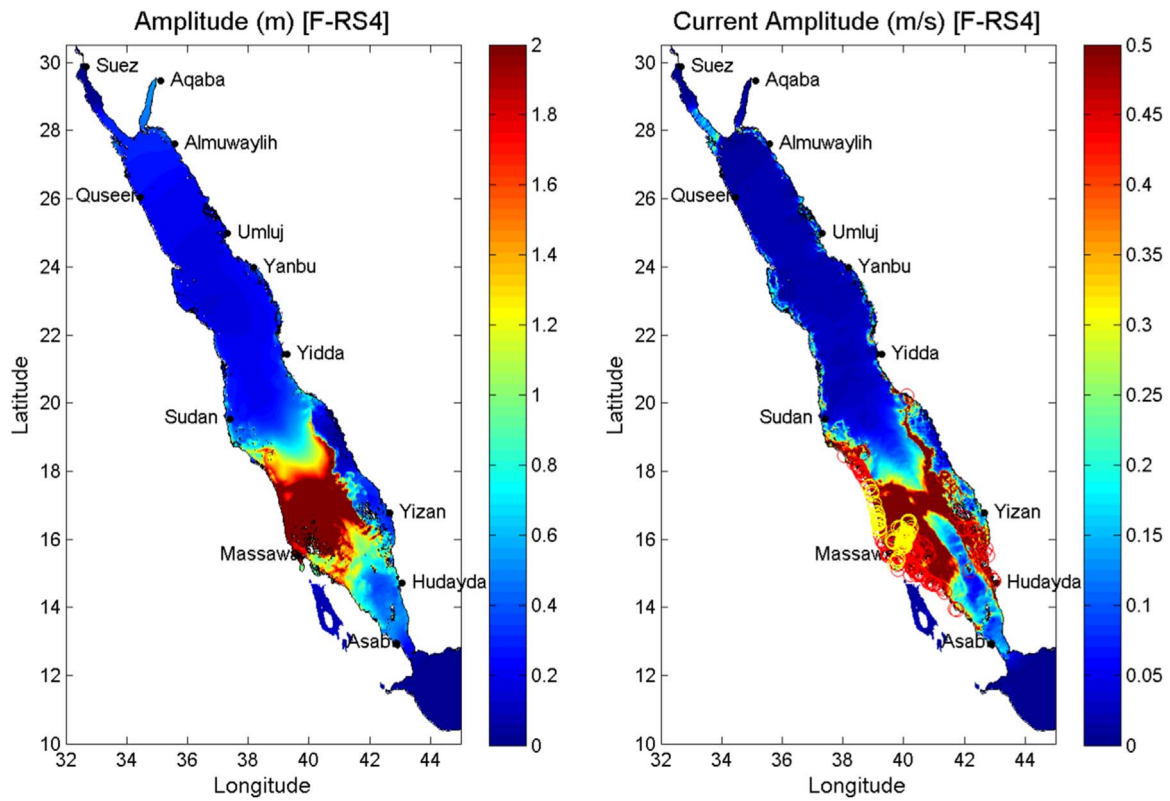
Fig. 9. As Fig. 6, but for tsunami F-RS4 (Table 1).

Tsunamis triggered by submarine earthquakes produce higher impacts in the shoreline than the set of studied events triggered by submarine landslides, entry of pyroclastic flows and volcano caldera collapse. The linear relationships found between peak energy and total flood volumes for the first group, along with the maps with the spatial distributions of maximum water elevation and current amplitudes, can
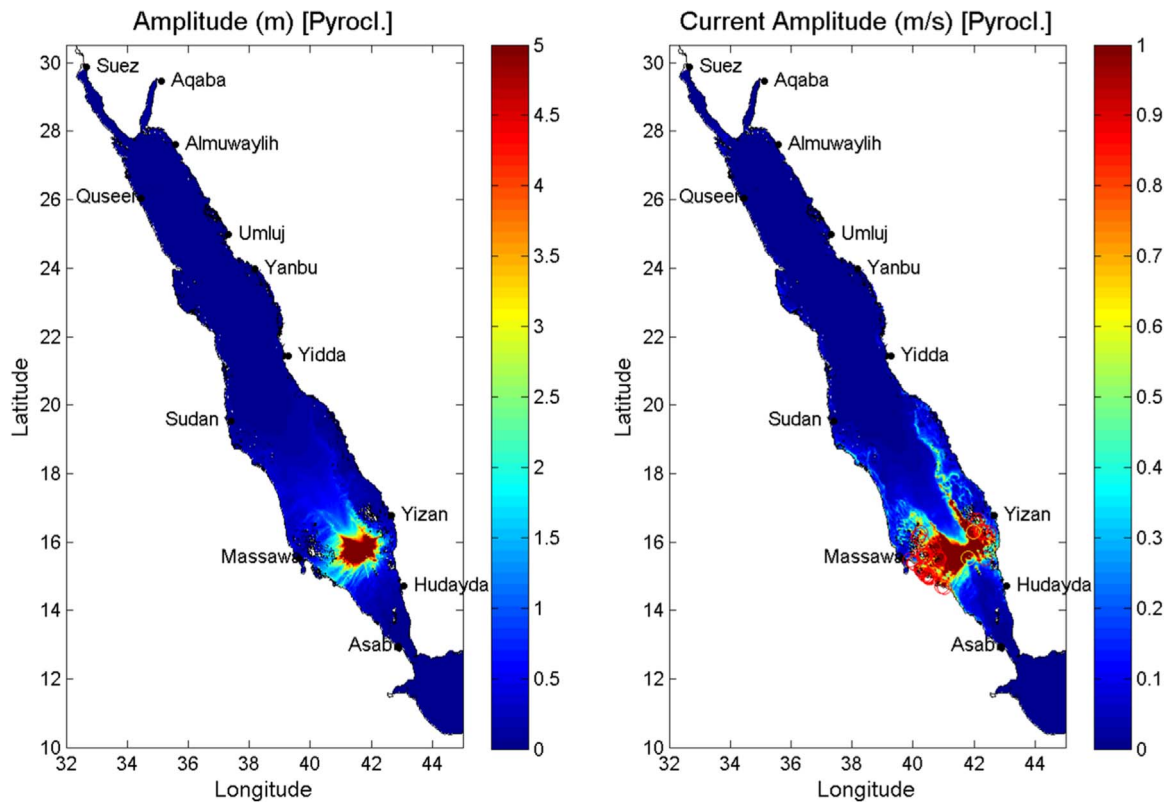

Fig. 10. Computed maximum amplitude for water elevation and water currents due to the entry of 5.4 km³ of pyroclastic flow (see text). Flooded area are depicted with the same criteria as in Fig. 6.
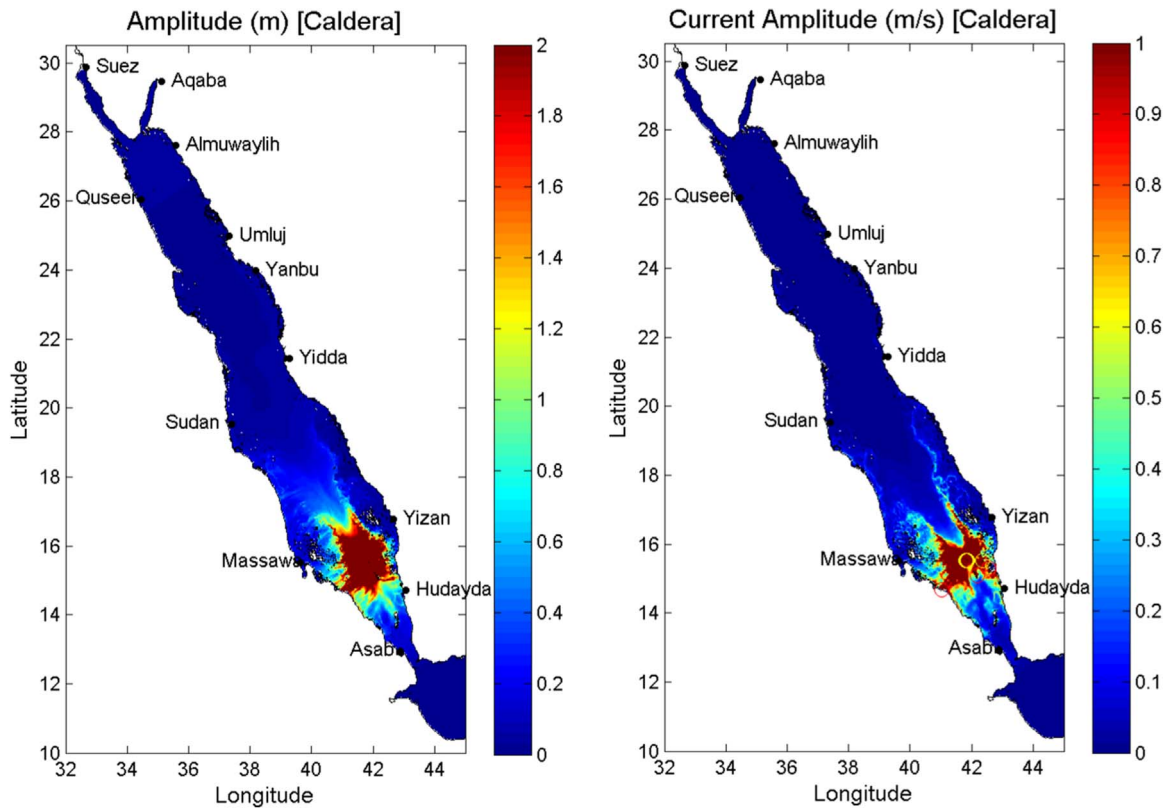
Fig. 11. Computed maximum amplitude for water elevation and water currents due to the simulated caldera collapse (see text). Flooded area are depicted with the same criteria as in Fig. 6.
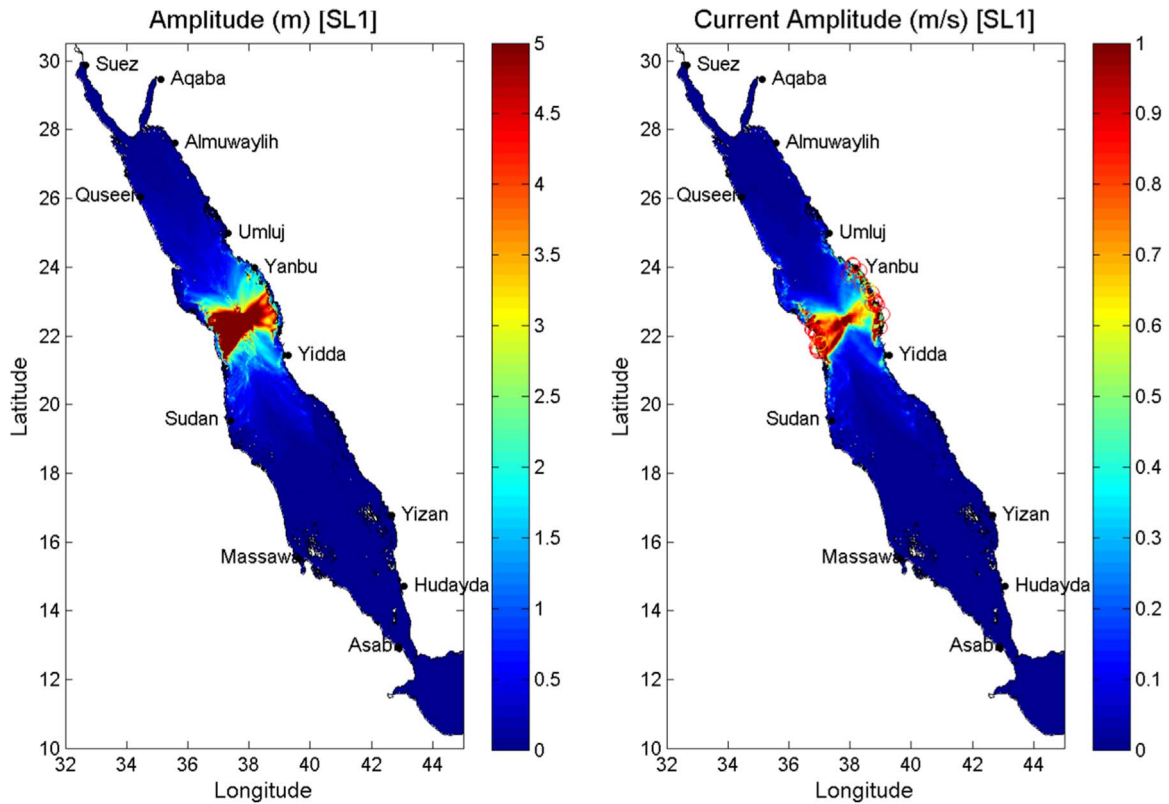

Fig. 12. As Fig. 6, but for the submarine landslide SL1 (Table 2).

be used to get a first proxy to the tsunami impacts. The tsunami hazard at any site of the Red Sea shoreline is primarily related with its proximity to the epicenter and with the tsunami peak energy.

Concerning the impacts on some strategic facilities, as the Suez Canal, present results show that tsunamis generated in the main Red Sea basin do not produce any noticeable effect along the shallow Gulf of

Table 3
Synthetic gauges used for FFT analysis.

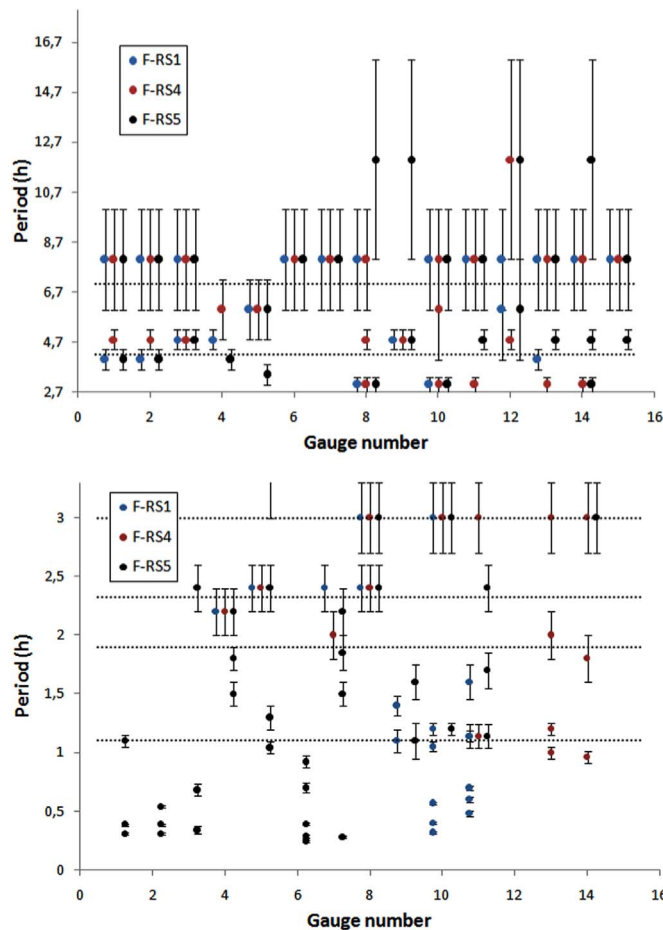| TG	Station	$\phi_E°$	$\lambda_N°$
1	Aqaba	34.995	29.524
2	Nuweiba	34.666	28.962
3	Sherm	34.329	27.842
4	Suez	32.533	29.933
5	Ras Ghareb	33.135	28.361
6	Quseer	34.328	26.102
7	Almuwaylih	35.453	27.676
8	Umluj	37.195	25.056
9	Yanbu	38.043	24.057
10	Yidda	39.153	21.495
11	Port Sudan	37.261	19.601
12	Yizan	42.540	16.850
13	Massawa	39.484	15.571
14	Al Hudayda	42.926	14.779
15	Asab	39.484	13.003

Fig. 13. Periods from FFT analysis for the 15 selected synthetic gauges (see Table 3, the index increases towards the Gulf of Aden). Horizontal lines corresponds to the expected periods for a rectangular open-mouth basin 2000 km long and with uniform depth 1150 m (n=1–5, n=9).

Suez. Even for events with epicenter in the gulf itself, as the source F-2, their impacts have a local character. Thus, the epicenter would have to be relatively close to the Suez Canal, but then, and as in the case of Nuweiba, the direct effects of the earthquake would likely be more noticeable than those due to the tsunami waves.

4. Conclusions

Results from the 1995-Nuweiba tsunami simulations are compa-

tible with the scarce observational data. Dispersive interferences, produced by the waves that are reflected along the shoreline, result in a "stormy sea" over which a pattern of standing waves arise, close to that expected for a open-ended rectangular basin of uniform depth with $T_0 \sim 2.7$ h.

A series of 12 potential tsunamigenic sources have been simulated. They are linked to submarine earthquakes, landslides and volcanos. Their spatial distributions cover the studied geographical domain, and their peak energies range from 1 kt up to 1.5 Mt. Their probability of occurrence cannot be assessed from historical records, although it can be guessed as very low. In all cases, the geometry of a narrow water-body promotes a fast energy dissipation in the nearby shorelines and prevents long distance impacts. Tsunamis with epicenter in the main Red Sea basin penetrate into the deep Gulf of Aqaba, where an amplification effect is observed for water elevations. Contrarily, in the relatively sallow Gulf of Suez the height of the tsunami waves is negligible, but water currents are enhanced.

The tsunamis triggered by submarine earthquakes showed a linear correlation between their peak energy (in the range from 0.8 up to 300 kt) and the global flooded volume at 99% confidence level and with slope 0.0157 ± 0.0006 km^3/kt. For these tsunamis, the related hazards at any site of the Red Sea shoreline is primarily related with its proximity to the epicenter and with the tsunami peak energy.

Tsunamis triggered by submarine earthquakes produce higher impacts in the shoreline than the set of studied events triggered by submarine landslides, entry of pyroclastic flows and volcano caldera collapse (e.g., their global flooded volumes were one order of magnitude higher).

A model of a rectangular open-mouth basin of uniform depth provides a gross understanding of the eigenmodes found with the spectral analysis carried out for the main Red Sea basin and the Gulfs of Suez and Aqaba. Thus, energetic tsunamis excite low frequency constituents with periods of 8 ± 2 h, 4.8 ± 0.4 h and 3.0 ± 0.3 h in the main basin, which can be interpreted as the eigenmodes for n=1,2,3. High frequencies are excited only in the proximity of the source, and the Gulf of Suez excites only those eigenmodes close to the ones of the main basin.

References

Abril, J.M., Periáñez, R., Escacena, J.L., 2013. Modelling tides and tsunami propagation in the former Gulf of Tartessos, as a tool for Archaeological Science. J. Archaeol. Sci. 40, 4499–4508.

Abril, J.M., Periáñez, R., 2015. The Minoan eruption of Thera and the parting of the Sea: a numerical modelling study on the potential role of tsunamis in the biblical Exodus. J. Mar. Sci. Eng. 3 (3), 745–771. http://dx.doi.org/10.3390/jmse3030745.

Alasset, P.J., Hébert, H., Maouche, S., Galbini, V., Meghraoui, M., 2006. The tsunami induced by the 2003 Zemmouri earthquake (MW=6.9, Algeria): modelling and results. Geophys. J. Int. 166, 213–226.

Al-Tarazi, E., 2000. The Major Gulf of the Aqaba earthquake, 22 November 1995 -maximum intensity distribution. Nat. Hazards 22, 17–27.

Ahmed, A.S.M., Abou-Elhaggag, M.E., El-Badry, H., 2012. Hydrodynamic modeling of the Gulf of Aqaba. J. Environ. Prot. 3, 922–934.

Baer, G., Funning, G.J., Shamir, G., Wright, T.J., 2008. The 1995 November 22, M_w, 7.2 Gulf of Elat earthquake cycle revisited. Geophys. J. Int. 175, 1040–1054.

Basta, N.Z., Salem, E.M., El Shahat, A.M., Habib, A.F., Ahamed, A.E., El Hakim, B.A., 1996. Seismicity of Gulf of Aqaba before and after Aqaba 95 quake. In: Proceedings of the Egyptian Geological Survey Cenn. Conference, 85 pp.

Bosworth, W., Huchon, Ph., McClay, K., 2005. The Red Sea and Gulf of Aden Basins. J. Afr. Earth Sci. 43, 334–378.

Cecioni, C., Bellotti, G., 2010. Modeling tsunamis generated by submerged landslides using depth integrated equations. Appl. Ocean Res. 32, 343–350.

Choi, B.H., Pelinovsky, E., Kim, D.Ch., Kim, K.O., Kim, K.H., 2008. Three-dimensional simulation of the 1983 central East (Japan) Sea earthquake tsunami at the Imwon Port (Korea). Ocean Eng. 35, 1545–1559.

d'Almeida, G.A.F., 2010. Structural evolution history of the red sea rift. Geotectonics 44 (3), 271–282.

Harbitz, C.B., 1992. Model simulations of tsunamis generated by the Storegga slides. Mar. Geol. 105, 1–21.

El Khrepy, S., Koulakov, I., Al-Arifi, N., 2015. Crustal Structure in the Area of the Cannon Earthquakes of Abu Dabbab (Northern Red Sea, Egypt), from Seismic Tomography Inversion. Bull. Seismol. Soc. Am. 105 (4), 13. http://dx.doi.org/10.1785/0120140333, (pp).

Feldens, P., Mitchell, N.C., 2015. Salt Flows in the Central Red Sea. In: Rasul, N.M.A., Stewart, I.C.F. (Eds.), The Red Sea. Springer, 12. http://dx.doi.org/10.1007/978-3-662-45201-1, (Earth System Sciences).

Finkl, Ch.W., Pelinovsky, E., Cathcart, R.B., 2012. A review of potential tsunami impacts to the Suez Canal. J. Coast. Res. 28 (4), 745–759.

Foster, A.N., Jackson, J.A., 1998. Source parameters of large African earthquakes: implications for crustal rheology and regional kinematics. Geophys. J. Int. 134, 422–448.

Iglesias, O., Lastras, G., Canals, M., Olabarrieta, M., González, M., Aniel-Quiroga, I., Otero, L., Durán, R., Amblas, D., Casamor, J.L., Tahchi, E., Tinti, S., De Mol, B., 2011. The BIG'95 submarine landslide-generated tsunami: a numerical simulation. J. Geol. 120, 31–48.

Ioualalen, M., Arreaga-Vargas, P., Pophet, N., Chlieh, M., Ilayaraja, K., Ordoñez, J., Renteria, W., Pazmiño, N., 2010. Numerical modelling of the 26th December 2004 Indian Ocean tsunami for the southeastern coast of India. Pure Appl. Geophys. 167, 1205–1214.

Jordan, B.J., 2008. Tsunamis of the Arabian Peninsula. A guide of historic events. Sci. Tsunami Hazards 27, 31–46.

Kampf, J., 2009. Ocean Modelling for Beginners. Springer-Verlag, Heidelberg.

Klinger, Y., Rivera, L., Haessler, H., Maurin, J.Chr., 1999. Active Faulting in the Gulf of Aqaba: new Knowledge from the M_w 7.3 Earthquake of 22 November 1995. Bull. Seismol. Soc. Am. 89 (4), 1025–1036.

Kowalik, Z., Murty, T.S., 1993. Numerical Modelling of Ocean Dynamics. World Scientific, Singapore.

Loncke, L., Gaullier, V., Droz, L., Ducassou, E., 2009. Multi-scale slope instabilities along the Nile deep-sea fan, Egyptian margin: a general overview. Mar. Pet. Geol. 26, 633–646.

Mascle, J., Benkhelil, J., Bellaiche, G., Zitter, T., Woodside, J., Loncke, L., Prismed II Scientific Party. 2000. Marine geologic evidence for a Levantine-Sinai Plate; a new piece of the Mediterranean puzzleGeol. (Boulder) 28 (9), 779–782.

Mitchell, N.C., Ligi, M., Ferrante, V., Bonatti, E., Rutter, E., 2010. Submarine salt flows in the central Red Sea Geological Society of America Bulletin 122, 701–713.

Mohamed, A.E.A., El-Hadidy, M., Deif, A., Abou Elenean, K., 2012. Seismic hazard studies in Egypt. NRIAG J. Astron. Geophys. 1, 119–140.

Monismith, S.G., 2004. Tides and sea level in the Gulf of Aqaba (Eilat). J. Geophys. Res. 109 (C04015), 6, (pp).

NGD, 2016. NGDCWDS Global Historical Tsunami Database. ⟨www.ngdc.noaa.govhazardtsu_db.shtml⟩. Last access on April 2016.

Novikova, T., Papadopoulos, G.A., McCoy, F.W., 2011. Modelling of tsunami generated by the giant Late Bronze Age eruption of Thera, South Aegean Sea, Greece. Geophys. J. Int. 186, 665–680.

Okada, Y., 1985. Surface deformation due to shear and tensile faults in a half-space. Bull. Seismol. Soc. Am. 75, 1135–1154.

Okal, E.A., Synolakis, C.E., Kalligeris, N., 2011. Tsunami simulations for regional sources in the South China and adjoining seas. Pure Appl. Geophys. 168, 1153–1173.

Periáñez, R., Abril, J.M., 2013. Modelling tsunami propagation in the Iberia-Africa plate boundary: historical events, regional exposure and the case-study of the former Gulf of Tartessos. J. Mar. Syst. 111–112, 223–234.

Periáñez, R., Abril, J.M., 2014a. Modelling tsunamis in the Eastern Mediterranean Sea. Application to the Minoan Santorini tsunami sequence as a potential scenario for the biblical Exodus. J. Mar. Syst. 139, 91–102.

Periáñez, R., Abril, J.M., 2014b. A numerical modelling study on oceanographic conditions in the former Gulf of Tartessos (SW Iberia): tides and tsunami propagation. J. Mar. Syst. 139, 68–78.

Rabinovich, A.B., 2009. Seiches and harbour oscillations. In: Kim, Y.C. (Ed.), Handbook of Coastal and Ocean Engineering. World Scientific Public, Singapore, 193–236.

Sahal, A., Roger, J., Allgeyer, S., Lemaire, B., Hebert, H., Schindelé, F., Lavigne, F., 2009. The tsunami triggered by the 21 May 2003 Boumerdes-Zmmouri (Algeria) earthquake: field investigations on the French Mediterranean coast and tsunami modelling. Nat. Hazards Earth Syst. Sci. 9, 1823–1834.

Salem, E.M., 2009. Paleo-Tsunami deposits on the Red Sea beach, Egypt. Arab J. Geosci. 2, 185–197.

Shaked, Y., Agnon, A., Lazar, B., Marco, S., Avner, U., Stein, M., 2004. Large earthquakes kill coral reefs at the north-west Gulf of Aqaba. Terra Nova 16, 133–138.

Torsvik, T., Paris, R., Didenkulova, I., Pelinovsky, E., Belousov, A., Belousova, M., 2010. Numerical simulation of a tsunami event during the 1996 volcanic eruption in Karymskoye lake, Kamchatka, Russia. Nat. Hazards Earth Syst. Sci. 10, 2359–2369.

Xu, W., Jónsson, S., 2014. The 2007-8 volcanic eruption on Jebel at Tair island (Red Sea) observed by satellite radar and optical images. Bull. Volcano. 76 (795), 14, (pp).

Xu, W., Ruch, J., Jónsson, S., 2014. Birth of two volcanic islands in the southern Red Sea. Nat. Commun. 6 (7104), 7, (pp).